Fiber-Optic Monitoring of a Twin Circular Shaft Excavation: Development of Circumferential Forces and Bending Moments in Diaphragm Walls

by

Shao-Qun LIN

PhD Student

Department of Civil and Environmental Engineering

The Hong Kong Polytechnic University, Hong Kong SAR, China

Email: shaoqun.lin@connect.polyu.hk

Dao-Yuan TAN (corresponding author)

Associate Professor

School of Earth Sciences and Engineering

Nanjing University, Nanjing, China

Email: dytan@nju.edu.cn

formerly,

Department of Civil and Environmental Engineering

The Hong Kong Polytechnic University, Hong Kong SAR, China

Yat Fai LEUNG

Associate Professor

Department of Civil and Environmental Engineering

The Hong Kong Polytechnic University, Hong Kong SAR, China

Email: andy.yf.leung@polyu.edu.hk

Jian-Hua YIN[1, 2]

Chair Professor of Soil Mechanics

[1]: Department of Civil and Environmental Engineering

[2]: Research Institute for Land and Space

The Hong Kong Polytechnic University, Hong Kong SAR, China

Email: cejhyin@polyu.edu.hk

Ivan LI
Geotechnical Engineer
Geotechnical Engineering Office
Civil Engineering and Development Department, Hong Kong SAR, China
Email: ivanli@cedd.gov.hk

Eric H.Y. SZE
Senior Geotechnical Engineer
Geotechnical Engineering Office
Civil Engineering and Development Department, Hong Kong SAR, China
Email: erichysze@cedd.gov.hk

Frankie L.C. LO
Senior Geotechnical Engineer
Geotechnical Engineering Office
Civil Engineering and Development Department, Hong Kong SAR, China
Email: frankielclo@cedd.gov.hk

Hon-Shing KAN
Deputy Project Manager
East Development Office
Civil Engineering and Development Department, Hong Kong SAR, China

Tommy C. W. WONG
Senior Engineer
East Development Office
Civil Engineering and Development Department, Hong Kong SAR, China

Eric Y. M. CHAN
Geotechnical Engineer
East Development Office
Civil Engineering and Development Department, Hong Kong SAR, China

Abstract: This study investigates the behaviour of a 38-m deep twin-circular ‘peanut-shaped’ cofferdam interconnected with a rectangular section for cut-and-cover tunnel construction, using distributed fibre optic sensors (DFOS) based on optical frequency domain reflectometry (OFDR). The distributed sensors revealed that temperature changes on the two sides of the diaphragm wall were different upon its exposure by excavation, while the measured strains were used to evaluate the wall deflection and bending moments. The high spatial resolution achieved by DFOS measurements revealed unique aspects of the wall response, which are difficult to be obtained by conventional types of instrumentation. In particular, the strains along vertical and lateral directions of the wall panels were measured, the latter of which indicated eccentric compression in the concrete panels that arise from the distinctive peanut-shaped geometry. Developments of hoop forces and circumferential bending moments in the panels at various construction stages are discussed, with particular focus on the release of such during partial demolition of a temporary crosswall to facilitate the assembly and launching of tunnel boring machines. The mechanisms of stress developments and release are simulated using three-dimensional finite element models which, together with the field measurements, enhance the understanding of the behaviour of multi-cell cofferdams.

Keywords: Circular cofferdam; Deep excavation; Diaphragm walls; Hoop strain; Distributed fibre optic sensors

Introduction

The design and construction of circular cofferdams are becoming common around the world, as they entail more working space within the excavation compared with multi-propped walls where the struts may obstruct the works. In some cases, wall toe stability could be enhanced by the circular geometry, reducing the needs for ground treatment below the excavation level. Therefore, the design of circular shafts often leads to more efficient and safer construction processes. Recently, Schwob et al. (2019) reported the construction of a 15-cell caterpillar-shaped cofferdam as part of a sub-sea road project in Hong Kong. Some cases of circular cofferdams have also been reported in the past. For example, Kumagai et al. (1999) measured the displacements and vertical and circumferential stresses of the retaining wall supporting a circular excavation with a diameter of 144 m. Parashar et al. (2007) reported the measurements of wall deflections and the circumferential stresses in three circular shafts with diameters of 30-40 m, while Tan & Wang (2013; 2015) studied the behaviour of a 100-m diameter circular cofferdam. Apart from circular shafts, elliptical or multi-cell excavations were adopted in some recent projects to facilitate the launching of tunnel boring machines (TBM). Gomes et al. (2008) reported the settlements and wall deflections for an elliptical excavation for Porto Light Metro, which was composed of two 22-m deep elliptic shafts (81 m × 40 m).

While it has been well established that the retaining structures of circular cofferdams depend on the hoop action to support the excavations, there is still considerable uncertainty regarding their behaviours, particularly the developments of circumferential (hoop) and bending stresses in the wall, and their relationships with the geomaterial properties and shaft geometry, especially in the case of imperfect circles such as elliptical or multi-cell caterpillar-shaped excavations. Despite the advances in numerical modelling software and design tools, there remains a need to monitor the various aspects of their performances, in order to enhance the understanding of such complex systems, ensure serviceability of nearby facilities and reduce conservatism in the design practice for similar project scenarios in the future. While ground settlements and vertical bending moments can be monitored through conventional instruments such as settlement markers or inclinometers, the measurements of circumferential forces or bending moments pose unique challenges. Diaphragm wall panels are usually around 2-3 m in width, and vibrating wire strain gauges only produce discrete measurements which may not be representative of the hoop stress distributions along the width of the panel. Under these conditions, distributed fibre optic sensors may prove to be the ideal technique. It has become increasingly popular for geotechnical and structural monitoring (Pelecanos et al., 2017; Nejjar et al., 2021; Sui et al., 2021), since they can achieve fully continuous sensing along the entire length of the sensing cable, without being disturbed by electromagnetic field and/or moisture. Successful applications of DFOS on excavation monitoring have been reported extensively. Li et al. (2018) utilized DFOS embedded in wall panels to investigate wall behaviour due to deep excavation, with the DFOS measurements in agreement with those by conventional inclinometers. Zhu et al. (2022) studied the deformation patterns of curved shield tunnels induced by adjacent excavations, based on the monitoring results by the DFOS. A summary of case studies of excavation monitoring using fibre optic sensing is presented in Table 1. Schwamb et al. (2014) and Torisu et al. (2019) presented the performance monitoring of circular excavations using distributed fibre optic sensors based on Brillouin optical time-domain reflectometry (BOTDR), but the spatial resolution was 1 m in their studies. The accuracy might therefore be compromised for the abovementioned range of wall panel widths. The lack of well-established instrumentation techniques for circumferential actions in these structures may have been an obstacle for the development of standards or guidelines regarding the alarm thresholds of such quantities during construction monitoring.

In this study, the behaviour of a “peanut-shaped” cofferdam comprising two connected circular excavations is investigated using distributed fibre optic sensors based on the optical frequency domain reflectometry (OFDR). The OFDR technology with a high spatial resolution of 5 cm was employed to improve the quality of the strain and temperature data, which is particularly important along the width of wall panel. The vertical curvatures, hoop forces and circumferential bending moments are investigated during various construction phases including dewatering, bulk excavation, installation of lateral supports, and partial structure demolition between the two circular sections. Three-dimensional numerical modelling shed further insights into the unique features of wall behaviour under these processes, further highlighting the importance of monitoring the developments of circumferential forces and bending moments in walls supporting circular or multi-cell excavations.

Project Background

The Trunk Road T2 and Cha Kwo Ling Tunnel Project of Hong Kong comprised a 3.4 km long, dual-two lane trunk road connecting the Central Kowloon Route to the West and the Tseung Kwan O-Lam Tin Tunnel to the East. Together they constituted Route 6 of the road network in the city. To facilitate the tunnelling operations, a TBM launching shaft was constructed, which comprised an approximately 22-m long cut-and-cover section of tunnel box connected to a 55-m long twin-circular cofferdam as shown in Fig. 1(a). Adjacent to the TBM launching shaft, there was an existing 4-storey building which housed the Public Works Central Laboratory and was founded on friction prestressed concrete piles. The clearance between the shaft wall and the building pile extrados was only 3.0 m. The twin-circular cofferdam comprised two open, strut-free circular cells with radii of about 22.0 m for Cell 1 and 19.5 m for Cell 2, respectively. This peanut-shaped geometry was preferred as it could enhance construction flexibility by eliminating steel struts, facilitate faster shaft excavation, assembly of the TBMs and construction of the permanent tunnel box structure, and significantly reduce impacts on adjacent structures and environment.

As indicated in Fig. 1(b), the rectangular section for cut-and-cover tunnel construction was laterally supported by five layers of concrete slabs, namely Slab 1 to Slab 4 and the base slab. There were two square openings for Slabs 1 to 4 with a side length of 9.0 m. Below Slab 4, two layers of preloaded steel struts were installed and then the western crosswall would be partially demolished between Slab 4 and the base slab, from -15.0 to – 28.0 mPD (metres above Hong Kong Principal Datum) for TBM assembly and launching. The diaphragm walls of the twin-circular cofferdam were designed to resist the water and soil pressures by developing hoop forces in compression transferred to four Y-panels. Two reinforced concrete (RC) beams were constructed at +2.5 mPD and -13.5 mPD, respectively, between Cell 1 and Cell 2 to enhance the lateral support. The eastern crosswall between Cell 1 and Cell 2 would be demolished simultaneously with the excavation process, down to the elevation of -25.0 mPD. The thickness of all diaphragm wall panels was 1.5 m. The construction sequences of the cut-and-cover tunnel section and the twin-circular cofferdam are shown in Figs. 2(a) and (b), while Fig. 2(c) shows the site photo after the bulk excavation stage.

The ground conditions at the site consisted of a layer of fill overlying a marine deposits (MD) layer and then alluvium (ALL) layer, as shown in Fig. 1(b). Completely decomposed granite (CDG) was encountered underneath the alluvium layer, while the bedrock was defined as Grade III or better rock (granite), and was generally encountered below -57 mPD across the site. The groundwater was encountered at around +2.0 mPD. The diaphragm wall panels of the cut-and-cover tunnel section were embedded into Grade III or better bedrock for groundwater cut-off while most of the wall panels of the twin-circular cofferdam were terminated above rockhead, and those adjacent to the Public Works Central Laboratory building were grouted to rockhead level for groundwater cut-off.

Optical Frequency Domain Reflectometry (OFDR)

The distributed strain and temperature sensing in this study is based on the optical frequency domain reflectometry (OFDR) technology. The working principle of the OFDR sensing system is illustrated in Fig. 3. Contrary to the optical time domain reflectometry (OTDR) technique, OFDR utilizes continuous waves of light sources to achieve higher signal-to-noise ratios. The incident light from a tunable laser source is divided into the reference light and the sensing light by an optical coupler. The former is reflected through a mirror, while the latter passes through the fibre optic sensing cable. Some portions of the sensing light experience Rayleigh backscattering due to variations in the refractive index in the fibre (Ding et al. 2018). The backscattered light is mixed with the reflected reference light by the optical coupler and then the mixed light is received and demodulated by a photoelectric detector to obtain the strain or temperature changes along the length of the fibre optic cable. Specifically, the Rayleigh spectral shift can be related to the strain and temperature changes by

$$\Delta v_R = c_\varepsilon \Delta\varepsilon_m + c_T \Delta T \quad (1)$$

where Δv_R is the Rayleigh spectral shift, $\Delta \varepsilon_m$ is the mechanical strain change in DFOS, ΔT is the temperature change in DFOS, c_ε is the coefficient of Rayleigh frequency shift induced by mechanical strain change, c_T is the coefficient of Rayleigh frequency shift induced by temperature change, c_ε and c_T can be considered as fixed values for single mode fibre under Rayleigh backscattering, which are -0.15 GHz/με and -1.25 GHz/K in OFDR system with 1550 nm bands (Leviton & Frey 2006; Wu et al. 2020). An OFDR-based interrogator (OSI-S) manufactured by Junlong Technology Ltd., Wuhan, China was used to collect the DFOS data in this study. The spatial resolution was set as 5 cm with measuring accuracy of ± 0.1 K or ± 1 με.

Installation of DFOS

Three types of fibre optic cables were used to monitor the behaviour of the diaphragm wall during excavation. A type of tight-buffered single-mode cable was employed for strain sensing (Fig. 4a), with the fibre core protected by a steel strand-reinforced, medium-density polyethylene (MDPE)-jacket. The cable diameter was 5.0 mm, where the tight buffer ensures efficient strain transfer and the steel strand reinforcement prevents the sensing fibre from being damaged during site activities such as hoisting of reinforcement cage and tremie concreting. A type of loose tube cable with a diameter of 5.0 mm was used to monitor the temperature changes (Fig. 4(b)). Surrounding the fibre core are four layers of filling materials including a spiral armour, Kevlar, metal mesh and a low smoke zero halogen (LSZH) sleeve that improve the robustness of the cable. The space between the optical fibre and the spiral armour makes it mechanical strain free. Both types of cables were manufactured by Suzhou NanZee Sensing Technology Ltd., China. A type of sensing cable (referred to as the LIOS cable in this study), manufactured by LIOS Sensing in Cologne, Germany, was also adopted and it involves optical fibres for both temperature and strain measurements within the same bundle, as shown in Fig. 4(c). The LIOS cable had a diameter of 10.9 mm.

Three panels were instrumented with fibre optic cables to investigate the behaviour of the twin-circular shaft excavation, as shown in Fig. 1(a). Panel 1 was located within the cut-and-cover tunnel section, while Panel 2 and Panel 3 were located within Cells 2 and 1, respectively. Specifically, Panel 1 was located near the center of the rectangular cut-and-cover tunnel section, where the bending moments along vertical direction and the deflections of the diaphragm wall were monitored. Panel 2 was located near the middle of circular Cell 2 where the purpose of DFOS instrumentation was to monitor the development of the circumferential forces far away from Y panels (heavily reinforced diaphragm wall panels to transmit hoop forces at the interface between Cell 1 and Cell 2, see Fig 1(a)). DFOS was also installed along the vertical direction of the wall panel to monitor the deflections, which was expected to be the largest deflection within Cell 2. Moreover, numerical simulations prior to the construction showed that partial demolition of the western crosswall would lead to releases of circumferential forces in nearby wall panels. Therefore, measurements at Panel 2 can be used to indicate the range and extent of such force release. Panel 3 was located near a Y panel and its response could reveal the hoop force transfer to the Y panel.

The cable arrangements for the three panels are illustrated in Fig. 5. In Panel 1, four strain sensing cables were installed along the depth of wall panel, arranged in pairs on the excavated side and the retained side of the wall, together with one temperature sensing cable installed on the excavated side for temperature compensation. In Panel 2, besides similar arrangements of the vertical strain sensing cables, an additional temperature sensing cable was installed on the retained side. Furthermore, two strain sensing cables were attached to the reinforcement cage in a zigzag pattern for Panel 2 and Panel 3 to monitor the hoop strains at various levels between -26.7 mPD and -35.0 mPD. In Panel 3, one set of temperature and strain sensing cable was installed to monitor the hoop strains between -26.9 mPD and -31.5 mPD on the retained side, while one LIOS cable (containing both strain and temperature sensing cables) was installed on the excavated side. For hoop strain monitoring in Panel 2 and Panel 3, there were a total of six and four horizontal sections on each side, respectively, with a length of about 2.0 m each. A pre-tension of 1000 $\mu\varepsilon$ was applied to the strain sensing cables to facilitate measurements of compressive strains through reductions in tension (Schwamb, 2014; ASTM F3079-14, 2014).

Data Processing

Temperature compensation

In this study, the temperature was determined by stress-free cables. There is a lump coefficient $c_{T,f} = c_T + \alpha_c c_\varepsilon$ for the stress-free cable (ASTM F3079-14, 2014). α_c is the coefficient of linear thermal expansion of the cable coatings and tight buffer. The values of $c_{T,f}$ of the NanZee and LIOS temperature sensing cables were obtained by water bath tests and found to be -4.38 GHz/K and -1.43 GHz/K, respectively. Therefore, the temperature can be evaluated by:

$$\Delta T = \frac{\Delta v_R}{c_{T,f}} \tag{2}$$

The measurements of strain sensing cables were affected by both mechanical strain and temperature changes. Contributions from the two components should be differentiated during the post-processing of raw data (Mohamad et al, 2011). The mechanical strain changes $\Delta\varepsilon_m$ of strain sensing cables include excavation-induced and concrete thermal-induced strains, and can be determined by

$$\Delta\varepsilon_m = \frac{1}{c_\varepsilon}\Delta v_R - \frac{c_T}{c_\varepsilon}\Delta T \tag{3}$$

The excavation-induced mechanical strain $\Delta\varepsilon'_m$ can be determined by

$$\Delta\varepsilon'_m = \Delta\varepsilon_m - \alpha_{con}\Delta T \tag{4}$$

where ΔT is the temperature change measured by the temperature sensing cable (Eq. (2)), α_{con} is the coefficient of linear thermal expansion of the concrete and is taken as $\alpha_{con} = 10\ \mu\varepsilon/\mathrm{K}$ (Browne, 1972).

Evaluation of curvature and internal forces

Assuming linear-elastic material behaviour for the reinforced concrete, the curvature and bending moment in the concrete wall panel can be evaluated by

$$\kappa_{zz} = \frac{\varepsilon_{zz\_e} - \varepsilon_{zz\_r}}{L} \tag{5a}$$

$$\kappa_{\theta\theta} = \frac{\varepsilon_{\theta\theta\_e} - \varepsilon_{\theta\theta\_r}}{L} \tag{5b}$$

$$M_{zz} = \frac{Et^3}{12(1-\nu^2)}(\kappa_{zz} + \nu\kappa_{\theta\theta}) \tag{5c}$$

$$M_{\theta\theta} = \frac{Et^3}{12(1-\nu^2)}(\kappa_{\theta\theta} + \nu\kappa_{zz}) \tag{5d}$$

where κ_{zz} and $\kappa_{\theta\theta}$ represent the curvatures in vertical and circumferential directions, respectively; ε_{zz_e} and ε_{zz_r} are the measured vertical strains on the excavated side and retained side, respectively; $\varepsilon_{\theta\theta\_e}$ and $\varepsilon_{\theta\theta\_r}$ are the measured horizontal or circumferential strains on the excavated side and retained side, respectively; L is the horizontal distance between sensing cables on the retained and excavated sides, which was 1.27 m in Panel 1 and 1.35 m in Panels 2 and 3 according to the site installation records; M_{zz} and $M_{\theta\theta}$ are the vertical and circumferential bending moments; the Young's modulus, E, was taken as 19.4 GPa considering the reduction in stiffness arising from the tremie concreting process, and cracking and creep effects in the concrete according to CIRIA C760 recommendations (Gaba et al. 2017); t is the thickness of the wall panel and is taken as 1.5 m; ν is the Poisson's ratio of the wall panel and is taken as 0.2. Positive values of curvature and bending moment indicate wall bending (convex) towards the excavation, as indicated in Fig. 5.

For Panel 1 of the cut-and-cover tunnel, M_{zz} is mainly contributed by κ_{zz} while $M_{\theta\theta}$ can be neglected considering the rectangular excavation geometry. For Panel 2 and Panel 3 within the circular cells, M_{zz} and $M_{\theta\theta}$ should include the contributions from both κ_{zz} and $\kappa_{\theta\theta}$. In this study, the DFOS installed in the vertical direction of Panel 1 and Panel 2 are able to obtain κ_{zz} induced by excavation. However, $\kappa_{\theta\theta}$ of Panel 2 and Panel 3 could only be determined at depths where hoop strains were measured, as indicated in Fig. 5(b). In that case, κ_{zz} instead of M_{zz} was discussed below for Panel 2.

The hoop forces F induced in Panel 2 and Panel 3 can be calculated by

$$\varepsilon_{zz} = \frac{\varepsilon_{zz\_e} + \varepsilon_{zz\_r}}{2} \tag{6a}$$

$$\varepsilon_{\theta\theta} = \frac{\varepsilon_{\theta\theta\_e} + \varepsilon_{\theta\theta\_r}}{2} \tag{6b}$$

$$F = \frac{Et}{1-\nu^2}(\nu\varepsilon_{zz} + \varepsilon_{\theta\theta}) \quad (6c)$$

where ε_{zz} and $\varepsilon_{\theta\theta}$ represent the vertical and circumferential normal strains of the wall panel, respectively. Positive values of strain and stress (and hence force) indicate tension. Since ε_{zz_e} and ε_{zz_r} of Panel 3 were not measured during excavation, $M_{\theta\theta}$ and F of Panel 3 presented below did not consider the contribution from the vertical direction.

Behaviour of the Diaphragm Wall Based on OFDR Data

Most of the fibre optic cables remained functional after the installation of diaphragm wall panels, except that the temperature sensing cable at Panel 1 was damaged at the elevation of -5.7 mPD after the concreting process (Fig. 5). As described in earlier sections, two bending strain sensing cables were installed on each side of the wall panels for redundancy. Since the measurements were very similar between the two cables on the same side, the following sections only present one set of data for each side of the wall.

Temperature changes

The hydration reaction of concrete generates considerable amounts of heat, causing significant temperature increase in the diaphragm wall panels after the concreting process. In this study, the benchmark readings for all fibre optic cables were taken shortly after concreting of the corresponding panels. Subsequent readings were compared against the benchmark to obtain strain and temperature changes during excavation. Therefore, temperature reductions are expected from the readings as heat was dissipated during concrete curing.

As indicated in Fig. 6(a), the temperature at Panel 1 decreased by an average of 6.3 K on the excavated side during excavation, two months after concreting. The temperature changes on both sides of Panel 2 are shown in Figs. 6(b) and (c). The temperature reductions, especially those on the excavated sides, were observed to be correlated to the excavation levels, and the temperature changes on the retained side and excavated side were notably different even at the same excavation stage. The temperature reduction reached 22.5 K on the excavated side, while the maximum reduction on the retained side was only 15.0 K. A possible reason for the difference could be the higher efficiency in heat convective loss from the concrete surface exposed to air compared to the heat conductive loss from the concrete to the surrounding soils. The similar phenomenon was also reported by Liou (1999), Kumagai et al. (1999) and Torisu et al. (2019). Therefore, it is important to conduct independent temperature monitoring on both sides of the diaphragm wall for respective temperature compensation using DFOS technique.

Curvature and bending moment

The temperature sensing cable in Panel 1 was damaged during construction. As a compromise, the measurements at -5.0 mPD of that cable were used for temperature compensation for evaluation of strains at Panel 1. Torisu et al. (2019) reported the temperature changes on the excavated and retained sides of diaphragm wall panels with thickness of 1.2 m and depth of 48 m, and stated that the temperature difference between the two sides were negligible after excavation, which was four months after the concreting process. In the current study, although errors might be introduced by imperfect temperature compensation at Panel 1, the estimated strains are deemed to produce reasonable estimates of the general trends of curvature in this panel at the final stage of excavation (Stage 7), which was reached nine months after concreting.

As shown in Fig. 7, the bending moment of Panel 1 was negligible at Stage 1, which indicated the first pumping test and dewatering had little effect on the wall deformation. As the excavation progressed, the maximum (positive) incremental bending moments occurred at depths that roughly coincided with the excavation levels from Stages 2 to 7. It is worth noting that negative values of incremental bending moments were observed at the levels of the slabs and preloaded steel struts from Stages 5 to 7.

The developments of vertical curvature κ_{zz} in Panel 2 are shown in Fig. 8. At Stage 1, no excavation work was conducted in Cell 2 except dewatering, although excavation of the adjacent cut-and-cover tunnel section had reached -10.0 mPD. The incremental curvatures were negligible at this stage. At Stages 2 and 3, the excavation reached -11.0 mPD and -16.0 mPD in Cell 2, respectively. An RC beam located at -13.5 mPD between Cell 2 and Cell 1 was constructed at the end of Stage 3. The positive incremental curvatures were observed above these two excavation levels. The positive incremental curvatures at Stages 4, 5 and 6 were significantly smaller than that at Stage 3, although the excavation progressed from -16.0 mPD to the final stage at -32.6 mPD. This could be attributed to the developments of hoop actions (to be elaborated later), together with the additional support provided by the RC beam. In addition, the eastern crosswall between the two cells remained at -25.0 mPD, which resisted the wall deformation at Stage 6.

Comparison of DFOS data and inclinometer data

In this section, the DFOS data are compared with inclinometer measurements regarding the wall curvatures in the vertical direction and lateral wall deflections. The inclinometer measurements at a panel opposite to Panel 1 (south side of cut-and-cover tunnel section) were used to compare with the fibre optics data since there was no inclinometer installed in Panel 1. On the contrary, inclinometer measurements were available at Panel 2 for direct comparisons with the DFOS technology. Based on Eq. (5a), the wall curvature can be directly estimated using the DFOS strain measurements from both sides of the panel. To estimate the wall deflection, double integration of the curvature requires two boundary conditions to be determined or assumed (Schwamb et al., 2016). In this study, the deflection at the wall bottom was assumed to be zero (same assumption for interpretation of inclinometer data), and the wall top deflection was assumed to be equal for DFOS and inclinometer data. It should be noted that the wall curvature profiles deduced by inclinometer readings sometimes involve unreasonable fluctuations when too few data points are used to determine the curvature. The phenomenon was observed in this study and was also reported by other researchers (Briaud et al. 2000; Tan & Wang 2015; Schwamb et al., 2016). To reduce data scattering and to capture the main trend of the wall curvature profile measured by inclinometer, data points of inclinometers for curvature calculation were selected with a depth interval (DI) of 2.5 m (original depth intervals of inclinometer readings were 0.5 m).

According to Fig. 9(a), both the fibre optic and inclinometer measurements showed that the maximum accumulative curvature occurred near the final excavation level of the cut-and-cover tunnel section. Negative values of curvature generally occur near the levels of slabs, with positive curvatures occurring in between. The curvature profiles deduced from the two independent devices matched well at most locations, except those values around -5.0 mPD and -45.0 mPD. As illustrated in Fig. 9(b), the maximum deflections evaluated from the inclinometer data and the fibre optic data were both located at the final excavation level, with magnitudes of about 42.6 mm and 38.5 mm, respectively. The difference can be attributed to the fact that the DFOS and inclinometer were in different panels and the geometry of the excavation was not exactly symmetric.

Figs. 10(a) and (b) present the accumulative curvature and wall deflection of Panel 2. The curvature profile derived from inclinometer measurements fluctuated significantly, especially below the final excavation level. On the contrary, the accumulative curvature profile calculated from the fibre optic data was more reasonable with the maximum values occurring around the RC beam level. Meanwhile, the locations of the maximum wall deflections obtained by two independent devices were similar with a magnitude of about 13 mm. Although the final excavation level in the two cells was deeper than that in the cut-and-cover tunnel, the deflections of Panel 2 were much smaller than those in Panel 1. This highlighted the advantage of circular excavations where more effective deformation control can be achieved with fewer lateral supports compared with excavation designs with conventional multi-propped walls.

The DFOS data after downsampling, including depth intervals (DI) of 1.0 m and 2.5 m, are also shown in Fig. 9(a) and Fig. 10(a). Downsampling from 'DI 0.05' to 'DI 2.5' reduced the data density and led to smoother wall curvatures over depth, especially at the final excavation level of Panel 1. In this study, the wall deflection was calculated using the DFOS data with a spatial resolution of 5 cm (DI 0.05), which prevented it from being underestimated after double integration of the curvature, as indicated in Fig. 9 (b) and Fig. 10 (b).

Hoop force and circumferential bending moment

The fibre optic cables were arranged in a zig-zag pattern on each side of Panel 2 and Panel 3 (Fig. 5), which allowed the measurement of hoop strains at six different depths in Panel 2 and four different depths in Panel 3, with a sensing length of 2.0 m in the horizontal direction. Temperature compensation for the measurements of each depth was achieved by using the 1-m average temperature data at the same depth of the temperature sensing cable. The hoop strain distributions along with sensing distance on both sides of Panel 2 are shown in Figs. 11(a) and (b). Six hoop strain sensing zones could be clearly identified. Contrary to the hoop strain measurements obtained by Schwamb et al. (2014) with a spatial resolution of 1.0 m, the hoop strain measurements in this study showed more details, which arose from the higher spatial resolution of 5 cm made possible by the OFDR technique.

To eliminate the possible boundary effects (Tan et al., 2021) near the two ends of the 2-m span and possible sensing length variations during the DFOS installation, only the strains within the middle 1 m of each span were averaged to represent the hoop strains at the corresponding depth. The development of hoop strains at different depths of both sides throughout construction is shown in Figs. 11(c) and (d). The compressive (negative) hoop strain between -26.7 mPD and -35.0 mPD of both sides gradually increased with the excavation process, indicating that Panel 2 was under circumferential compression throughout excavation.

The development of average hoop force and circumferential bending moment of Panel 2 is presented in Figs. 12(a) and (b). After Stage 1, compressive hoop force and positive bending moment were observed in Panel 2 due to the combined effects of the excavation in the adjacent cut-and-cover tunnel section and the dewatering operations in the peanut-shaped shaft. The excavation work in the cells commenced from Stage 2 and the excavation level reached -21.0 mPD at Stage 4. The compressive hoop forces and circumferential bending moments at six monitoring positions increased synchronously with the excavation, which indicated that Panel 2 was under eccentric compression. At Stage 5, the excavation reached about -27.0 mPD and the western crosswall was demolished from -15.0 mPD to -27.0 mPD in the meantime. Although the excavation was ongoing at this stage, both the compressive hoop force and circumferential bending moment stayed almost constant at the start of Stage 5. These may be attributed to the partial demolition of the western crosswall in this stage, which hampered the development of hoop action and altered the path of load transfer around the individual panels constituting the peanut-shaped structure. Some of the compressive hoop forces were therefore released in Panel 2 during this construction stage, together with the circumferential bending moments. At Stage 6, the excavation reached the final excavation level. The compressive hoop force increased again and eventually became stable, while the circumferential bending moment generally remained stable. Figs. 12(c) and (d) show the monitoring results at Panel 3, where the developments of compressive hoop forces and circumferential bending moments before Stage 5 were consistent with those of Panel 2, but the internal forces kept increasing during Stage 5. This indicated that the crosswall demolition did not have significant impacts on Panel 3, which was located further away from the western crosswall.

Numerical Analysis on Development of Hoop Force and Circumferential Bending Moment

A series of numerical analyses have been performed to enhance the understanding on the behaviour of diaphragm wall around the twin-circular cofferdam. The purpose of these is not to back-analyse the system performance or calibrate material parameters. Instead, the goals of these simulations are twofold: (i) to demonstrate the redistribution of hoop forces as the ‘circular’ geometry is broken up by the partial demolition of crosswall; and (ii) to highlight the importance of hoop strain measurements in walls supporting excavation using twin-circular or other multi-cell cofferdams, as they can be important performance indicators of the effectiveness of lateral support system that are also related to deformations of nearby ground and structures. The simulations presented in this study are performed using the finite element modelling software PLAXIS 3D. The subsurface strata and model dimensions are shown in Fig. 13(a). The diaphragm wall panels and slabs in the cut-and-cover tunnel section and peanut-shaped cofferdam are modelled using isotropic elastic shell elements while the capping beams, Y panels and steel walers are modelled using beam elements, as shown in Fig. 13(b). The preloading forces of the two layers of steel struts are modelled as linearly distributed loads transferred to the walers, with values of 1640 and 1460 kN/m (from site measurement), respectively. The loadings from nearby existing facilities are also considered in the model. Tables 2 to 4 present the input parameters for the numerical models, which are extracted from geotechnical investigation of the site and other published studies on local soil properties (e.g., Ng et al., 2014). In total, four numerical models are generated to investigate different scenarios. The benchmark model adopts parameters and modelling stages that closely resemble the actual construction conditions, while three additional models are created for a parametric study on the effects of partial demolition of western crosswall. Case 1 models the scenario where the crosswall demolition does not take place; Case 2 involves demolition of a larger extent of the wall (-4 to -15 mPD); Case 3 simulates the effects of reduced stiffness in the wall panels along the circumferential direction, which may arise from panel misalignment, imperfect connections between the panels or other construction defects. This is similar to a scenario described by Aye et al. (2014), on the issue of deviation of wall alignment that would lead to additional eccentricity due to non-circularity of the shaft.

In the benchmark case, two panels around Cell 2 are marked as ‘L’ and ‘M’, to indicate the leftmost and middle panels in that section, as shown in Fig. 13(b). The development of internal forces at -26.7 mPD of these panels in the benchmark model are shown in Fig. 14. The partial demolition of the western crosswall affects the development of hoop action around Cell 2, causing redistribution of hoop forces and bending moments in the wall panels. In particular, significant release of the compressive hoop forces in Panel ‘L’ is observed, while those in Panel ‘M’ are also mildly affected. The circumferential bending moments in these two panels are also reduced during the process, with the effect attenuating gradually with distance away from the western crosswall. The DFOS measurement data at -26.7 mPD of Panel 2 are also presented in Fig. 14, which indicates that the numerical results generally capture the trends of hoop force and circumferential bending moment developments in Panel 2, especially the hoop force and bending moment release during Stage 5 of the construction. The discrepancies between the measured data and numerical results can be partly attributed to non-uniform water levels and excavation progress across the actual construction site which could not be fully captured in the numerical simulations. In addition, the effect of the crosswall demolition on the hoop force and circumferential bending moment of Panel 3 was insignificant in the benchmark model, which is consistent with the DFOS measurements shown in Fig. 12(c) and (d).

Compared with the benchmark case, the hoop forces at Panel 'L' are about 20% larger in Case 1, as shown in Figs. 15(a) and (c). This again indicates the effect of crosswall demolition (in benchmark model) on the release of hoop force. As the hoop action develops more effectively in Case 1, the wall deflections are approximately 10% smaller compared with the benchmark model (Figs. 15(b) and (d)). On the contrary, Case 2 simulates a larger section of the crosswall being removed, which leads to the release of hoop forces in a wider extent of the nearby Panel 'L'. Perhaps more importantly, the deflection at that panel also increases by more than 20% at some locations. The more extreme scenario modelled in Case 3 leads to even more significant reduction of hoop forces in the entire panel, while the wall deflection increases by 40 to over 80% along the depth of the panel. In general, since circular or multi-cell cofferdams rely on the hoop action in wall panels for overall stability, under-development of such could result in excessive wall deflections and hence ground settlements in the vicinity. Therefore, hoop strain monitoring based on DFOS would provide important indications or even early warning of unexpected system performance.

Discussions

The DFOS used in this study revealed both the deflection profiles of individual diaphragm wall panels around the shaft and the strains and bending moments developed in various directions as excavation progressed. The measurements of hoop forces and circumferential bending moments are particularly important for circular or multi-cell cofferdams which utilize hoop action as the main support mechanism in lieu of steel struts as in rectangular cofferdams. In other words, monitoring of hoop action through lateral strains in wall panels serves a similar purpose as strut force monitoring in multi-propped excavations, as the development of support forces and nearby ground movements are often intertwined: there had been previous cases where ground collapse shortly followed unexpected and sudden losses of the measured support forces. High-resolution distributed strain sensing technique was not available in the past, which hampered the implementation of lateral strain monitoring of concrete wall panels. Following the success of this pilot study, future investigations on hoop strain developments could lead to wider adoption of systematic guidelines of alarm thresholds of such for circular or multi-cell cofferdams.

Based on the measurements and numerical results in this study, the instrumented panels for hoop force monitoring can be selected according to three criteria. The first criterion is to identify and monitor wall panels with the maximum hoop forces or circumferential bending moments induced by excavation, according to numerical analyses in the design stage. The second one is to monitor the wall panel that may be greatly impacted by construction activities such as local wall demolition, local surcharge, and nearby excavations or tunnelling operations. In addition, the monitoring positions can be set where significant eccentric stresses are expected in the circumferential direction, arising from the complex multi-cellular geometries or cofferdams that are not perfectly circular in shape.

Conclusions

This paper investigates the response of a twin-circular, peanut-shaped cofferdam using distributed fibre optic sensing technique with a high spatial resolution. This revealed the detailed developments in hoop action in individual wall panel, including their hoop forces and circumferential bending moments, during the complex construction process. The key findings are summarized as follows:

(a) The wall panels of the peanut-shaped cofferdam were under eccentric compression throughout the excavation. Partial demolition of the crosswall influenced the hoop action and released some of the compressive hoop forces and circumferential bending moments in wall panels. These details are difficult to be captured using conventional instruments. More obvious hoop force release is expected in wall panels near the location of wall demolition.

(b) Hoop strain monitoring based on DFOS for circular or multi-cell excavations can provide useful information to validate the design assumptions or compare with design predictions. The monitoring results also give indications of stress variations of the monitored wall panels due to localised disturbance of the cofferdam during construction.

(c) Comparisons between the performances of Panel 1 and Panel 2 showed that smaller wall deflections developed in the twin-circular cofferdam even though it supported a deeper excavation with fewer lateral supports installed, as compared to the rectangular multi-propped section. This demonstrates the effectiveness of utilizing hoop action to support the excavation.

(d) Temperature changes in the diaphragm wall were different between the excavated and retained sides during excavation, especially shortly after concrete placement. This could be attributed to the higher efficiency in heat convective loss from the surface exposure to air compared with the heat conductive loss from the concrete surface to the surrounding soil strata. Therefore, installation of temperature sensing cables on both sides of the wall is recommended if DFOS is used for monitoring.

There are few reported field applications of DFOS techniques with high spatial resolution in geotechnical monitoring. For certain geotechnical infrastructure, the monitoring accuracy might be compromised or insufficient if the spatial resolution of measurements is low. Compared with conventional discrete instruments or DFOS with low spatial resolution, the OFDR technology adopted in this study can provide more details in performance monitoring. These details would facilitate the analyses and enhance the understanding on the behaviour of geotechnical structures, including piles, tunnels and other complicated structures with circular or elliptical geometries, where hoop force development and the induced displacements are of great importance.

Data Availability Statement

All monitoring data and numerical results that support the findings of this study are available from the corresponding author upon reasonable request.

Acknowledgments

This paper is published with the permission of the Director of Civil Engineering and Development, the Head of the Geotechnical Engineering Office, and the Project Manager of the East Development Office of the Government of the Hong Kong SAR, China. The work presented in this paper is supported by Research Impact Fund (RIF) project (R5037-18), a Theme-based Research Scheme Fund (TRS) project (T22-502/18-R), and four General Research Fund (GRF) projects (PolyU 152179/18E; PolyU 152130/19E; PolyU 152100/20E; 15222021) from Research Grants Council (RGC) of Hong Kong Special Administrative Region Government of China. The authors also acknowledge the financial supports from grants (CD82 and CD7A) from Research Institute for Land and Space, and grants (ZDBS, BD8U) from The Hong Kong Polytechnic University.

References

ASTM. 2014. Standard practice for use of distributed optical fiber sensing systems for monitoring the impact of ground movements during tunnel and utility construction on existing underground utilities. F3079-14, West Conshohocken, PA.

Aye, T. T., Tong, M. S. Y., Yi, K. H., and Arunasoruban, E. 2014. "Design and construction of large diameter circular shafts." In *Underground Singapore*. Tunnelling and Underground Construction Society.

Browne, R. D. 1972. "Thermal movement in concrete." Concrete 6 (11): 51-53.

Briaud, J. L., Nicholson, P., and Lee, J. 2000. "Behavior of full-scale VERT wall in sand." *J. Geotech. Geoenviron. Engng.* 126 (9): 808-818. https://doi.org/10.1061/(ASCE)1090-0241(2000)126:9(808)

Ding, Z., Wang, C., Liu, K., Jiang, J., Yang, D., Pan, G., ..., and Liu, T. 2018. "Distributed optical fiber sensors based on optical frequency domain reflectometry: A review." *Sensors* 18 (4): 1072. https://doi.org/10.3390/s18041072

Gomes, A. T., Cardoso, A. S., Sousa, J.A., Andrade, J.C., and Campanhã, C. A. 2008. "Design and behavior of Salgueiros station for Porto metro." *6th International conference on case histories in geotechnical engineering.* 1-12. Scholars' Mine, Missouri University of Science and Technology. https://scholarsmine.mst.edu/icchge/6icchge/session08c/6

Gaba, A., Hardy, S., Doughty, L., Powrie, W., and Selemetas, D. 2017. *Guidance on embedded retaining wall design (C760)*. London: Construction Industry Research and Information Association.

Kumagai, T., Ariizumi, K., and Kashiwagi, A. 1999. "Behaviour and analysis of a large-scale cylindrical earth retaining structure." *Soils Found.* 39 (3): 13-26. https://doi.org/10.3208/sandf.39.3_13

Liou, D. D. 1999. "Thermal effects in large-sized diaphragm wall." *J. Perform. Constr. Facil.* 13 (1): 17-21. https://doi.org/10.1061/(ASCE)0887-3828(1999)13:1(17)

Leviton, D. B., and Frey, B. J. 2006. "Temperature-dependent absolute refractive index measurements of synthetic fused silica." In Vol. 6273 of Optomechanical technologies for astronomy, 800–810. Bellingham, WA: Society of Photo-Optical Instrumentation Engineers.

Li, Z., Soga, K., and Kechavarzi, C. 2018. "Distributed fibre optic sensing of a deep excavation adjacent to pre-existing tunnels." *Géotechnique Letters* 8 (3): 171-177. https://doi.org/10.1680/jgele.18.00031

Mohamad, H., Soga, K., Pellew, A., and Bennett, P. J. 2011. "Performance monitoring of a secant-piled wall using distributed fiber optic strain sensing." *J. Geotech. Geoenviron. Engng.* 137 (12): 1236-1243. https://doi.org/10.1061/(ASCE)GT.1943-5606.0000543

Ng, C. W. W., Leung, A. K., Kwok, S. S. K., and Yip, F. H. T. 2014. "Effects of stiffness nonlinearity on E' standard penetration test N correlations for analysing wall deflections in Hong Kong excavations." *HKIE Transactions* 21 (1): 35-49. https://doi.org/10.1080/1023697X.2014.884968

Nejjar, K., Dias, D., Cuira, F., Chapron, G., and Lebissonnais, H. 2021. "Experimental study of the performance of a 32 m deep excavation in the suburbs of Paris." *Géotechnique* 1-11. https://doi.org/10.1680/jgeot.21.00017

Parashar, S., Mitchell, R., Hee, M. W., Sanmugnathan, D., and Nicholson, G. 2007. "Performance monitoring of deep shafts at Changi WRP project, Singapore." In *Proc. 7th FMGM 2007: Field Measurements in Geomechanics,* 1-12. Reston, VA: ASCE.

Pelecanos, L., Soga, K., Chunge, M. P., Ouyang, Y., Kwan, V., Kechavarzi, C., and Nicholson, D. 2017. "Distributed fibre-optic monitoring of an Osterberg-cell pile test in London." *Géotechnique Letters* 7 (2): 152-160. https://doi.org/10.1680/jgele.16.00081

Pei, H., Yin, J., and Wang, Z. 2019. "Monitoring and analysis of cast-in-place concrete bored piles adjacent to deep excavation by using BOTDA sensing technology". *J. Mod. Optic.* 66 (7): 703-709. https://doi.org/10.1080/09500340.2018.1559948

Schwamb, T., Soga, K., Mair, R. J., Elshafie, M. Z. E. B., Sutherden, R., Boquet, C., and Greenwood, J. 2014. "Fibre optic monitoring of a deep circular excavation." *Proc. Instn Civ. Engrs - Geotech. Engng.* 167 (2): 144-154. https://doi.org/10.1680/geng.13.00036

Schwamb, T. 2014. “Performance monitoring and numerical modelling of a deep circular excavation.” Ph.D. thesis, Dept. of Engineering, Univ. of Cambridge.

Schwamb, T., Elshafie, M. Z. E. B., Soga, K., and Mair, R. J. 2016. “Considerations for monitoring of deep circular excavations.” *Proc. Instn Civ. Engrs - Geotech. Engng.* 169 (6): 477-493. https://doi.org/10.1680/jgeen.15.00063

Schwob, A., Cagnat, E., Chen, S., Chan, A. W., and Ng, C. C. 2019. “Tuen Mun–Chek Lap Kok Link: an outstanding subsea tunnel project in Hong Kong.” *Proc. Instn. Civ. Engrs – Civ. Engng.* 173 (5): 33-40. Thomas Telford Ltd. https://doi.org/10.1680/jcien.19.00027

Song, H., Pei, H., and Zhu, H. 2021. “Monitoring of tunnel excavation based on the fiber Bragg grating sensing technology.” *Measurement* 169: 108334. https://doi.org/10.1016/j.measurement.2020.108334

Sui, Y., Cheng, X., and Wei, J. 2021. “Distributed fibre optic monitoring of damaged lining in double-arch tunnel and analysis of its deformation mode.” *Tunnelling Underground Space Technol*. 110: 103812. https://doi.org/10.1016/j.tust.2021.103812

Tan, Y., and Wang, D. 2013. “Characteristics of a large-scale deep foundation pit excavated by the central-island technique in Shanghai Soft Clay. I: bottom-up construction of the central cylindrical shaft.” *J. Geotech. Geoenviron. Engng.* 139 (11): 1875-1893. https://doi.org/10.1061/(ASCE)GT.1943-5606.0000928

Tan, Y., and Wang, D. 2015. “Structural behaviors of large underground earth-retaining systems in Shanghai. I: Unpropped circular diaphragm wall.” *J. Perform. Constr. Facil.* 29 (2): 04014058. https://doi.org/10.1061/(ASCE)CF.1943-5509.0000521

Torisu, S. S., Faustin, N. E., Elshafie, M. Z. E. B., Black, M., Soga, K., and Mair, R. J. 2019. “Monitoring of Shaft Excavations in Clay.” *In Proc., Int. Conf. on Smart Infrastructure and Construction 2019 (ICSIC) Driving Data-Informed Decision-Making, 655–664. London: Institution of Civil Engineers.*

Tan, X., Bao, Y., Zhang, Q., Nassif, H., and Chen, G. 2021. “Strain transfer effect in distributed fiber optic sensors under an arbitrary field.” *Automat. Constr.* 124: 103597. https://doi.org/10.1016/j.autcon.2021.103597

Wang, F., Zhang, D. M., Zhu, H. H., Huang, H. W., and Yin, J. H. 2013. “Impact of overhead excavation on an existing shield tunnel: field monitoring and a full 3D finite element analysis.” *Comput. Mater. Con.* 34 (1): 63-81.

Wu, J., Liu, H., Yang, P., Tang, B., and Wei, G. 2020. “Quantitative strain measurement and crack opening estimate in concrete structures based on OFDR technology.” *Opt. Fiber Technol.* 60: 102354. https://doi.org/10.1016/j.yofte.2020.102354

Zhu, H. H., Wang, D. Y., Shi, B., Wang, X., and Wei, G. Q. 2022. “Performance monitoring of a curved shield tunnel during adjacent excavations using a fiber optic nervous sensing system.” *Tunnelling Underground Space Technol*. 124: 104483. https://doi.org/10.1016/j.tust.2022.104483

Table 1. Summary of case studies of excavation monitoring using fibre optic sensing

Structure	Monitoring parameters	Technique	Site location	Installation method	Reference
Secant-piled wall	Strain and temperature	BOTDR	London, UK	Embedded in the secant-piled wall	Mohamad et al. (2011)
Existing tunnel	Tunnel displacement	FBG	Shanghai, China	Adhered to the PVC tube by epoxy resin	Wang et al. (2013)
Diaphragm wall	Bending and circumferential hoop strains	BOTDR	London, UK	Embedded in the wall panels	Schwamb et al. (2014)
Diaphragm wall	Strains at the soil side and the excavation side	BOTDR	London, UK	Embedded in the wall panels	Li et al. (2018)
Diaphragm wall	Bending and thermal strains	BOTDR	London, UK	Embedded in the wall panels	Torisu et al. (2019)
Bored pile	Strain and temperature	BOTDA	Hong Kong, China	Embedded in the piles	Pei et al. (2019)
Gypsum pile	Soil deformation	FBG	Model test	Attached to the piles	Song et al. (2021)
Tunnel linings	Longitudinal and circumferential strains	BOFDA	Suzhou, China	Point-to-point fixing using steel clamps	Zhu et al. (2022)

BOTDR: Brillouin optical time-domain reflectometry; FBG: Fibre Bragg grating; BOTDA: Brillouin optical time domain analysis; BOFDA: Brillouin optical frequency domain analysis.

Table 2. The geotechnical parameters of strata in the design report

Stratum	γ: kN/m^3	SPT-N	E: MPa	c: kPa	ϕ: degrees	c_u: kPa	E_u: MPa
Fill	19.0	10	15.0	0.0	33.0	/	/
MD	19.0	4	6.0	0.0	28.0	20.0	10.0
All	19.0	18	27.0	0.0	36.0	/	/
		$2.75 \times (D - 22) + 18$	$4.125 \times (D - 22) + 27$				
CDG	19.0	$0.7 + 1.62D$	150.0	5.0	38.0	/	/

Note: D = depth below ground level; and SPT-N = N-value of the standard penetration test.

Table 3. Input geotechnical parameters

Stratum	Models	γ: kN/m^3	E: MPa	ν	c'_{ref}: kPa	ϕ': degrees	E_{50}^{ref}: MPa	E_{oed}^{ref}: MPa	E_{ur}^{ref}: MPa	m	p^{ref}: kPa	$\gamma_{0.7}$: %	G_0^{ref}: MPa
Fill	HSS	19.0	/	/	0.1	32.0	25.0	20.0	75.0	0.5	27.0	0.0012	105.0
MD	HS	19.0	/	/	0.1	28.0	7.8	13.5	23.4	0.5	50.0	/	/
ALL	HS	19.0	/	/	0.1	36.0	24.0	24.0	75.0	1.0	200.0	/	/
CDG	HSS	19.0	/	/	0.1	35.0	40.0	32.0	120.0	0.5	30.0	0.0016	98.0
Bedrock	LE	24.0	5000.0	0.2	/	/	/	/	/	/	/	/	/

MD: marine deposit; All: alluvium (sand); CDG: completely decomposed granite.
HS: Hardening Soil model; HSS: Hardening Soil model with small-strain stiffness; LE: Linear elastic.

Table 4. Input structure parameters

Structures	t: m	γ: kN/m^3	E: GPa	ν	A: m^2
Capping beam	/	6.0*	18.5	/	6.0
RC beam	/	24.5	21.0	/	5.0
Y-panel	/	6.0*	20.2	/	15.6
Diaphragm wall	1.5	6.0*	19.4	0.2	/
Crosswall	1.5	6.0*	19.4	0.2	/
Slab 1~ Slab 4	1.5	24.5	18.5	0.2	/
Base slab	2.0	24.5	18.5	0.2	/
Steel waler	/	78.0	210.0	/	0.07

*To accurately reflect the stress experienced by the soil beneath concrete structures, the unit weight of the concrete structures was reduced by the weight of the soil.

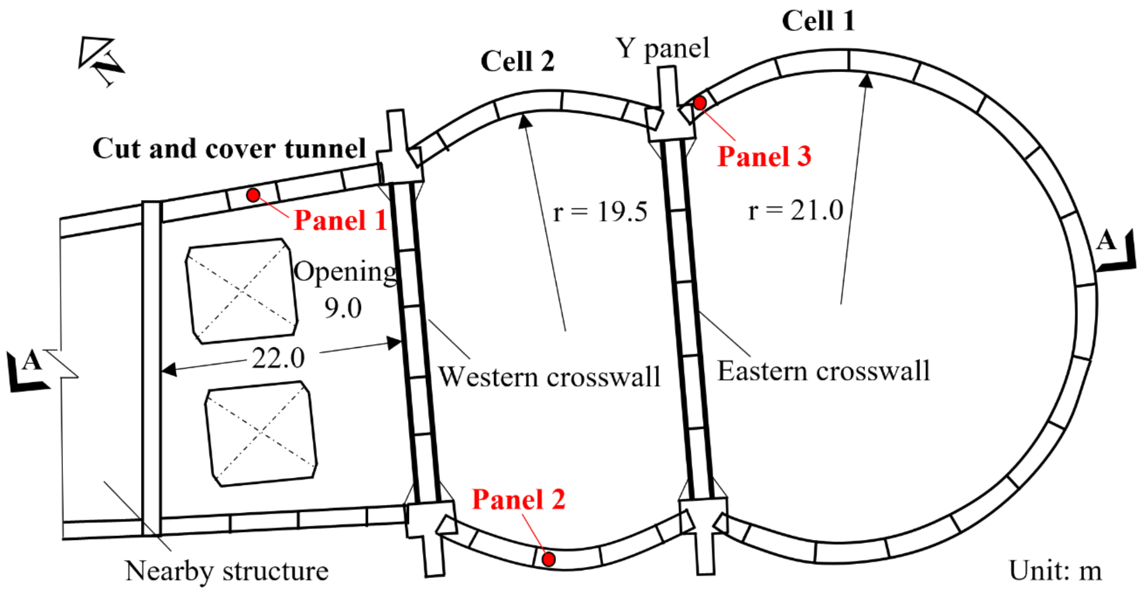

(a)

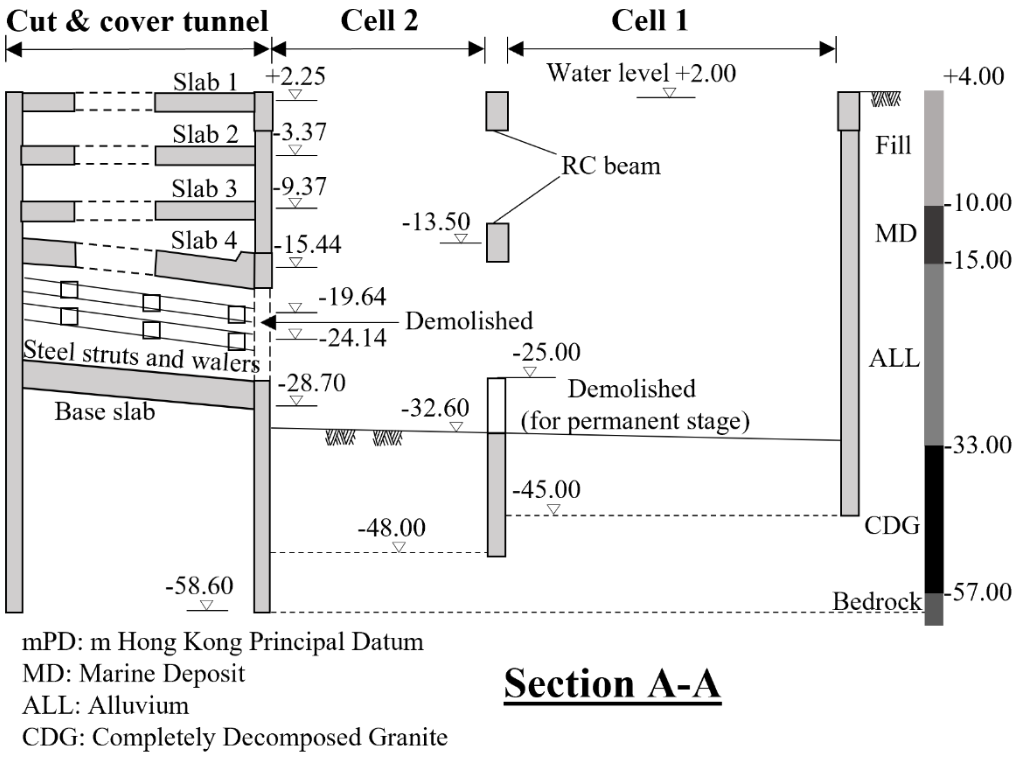

(b)

Fig. 1. (a) Sketch of the cofferdam with instrumented panels; (b) cross-section and ground conditions of the cofferdam

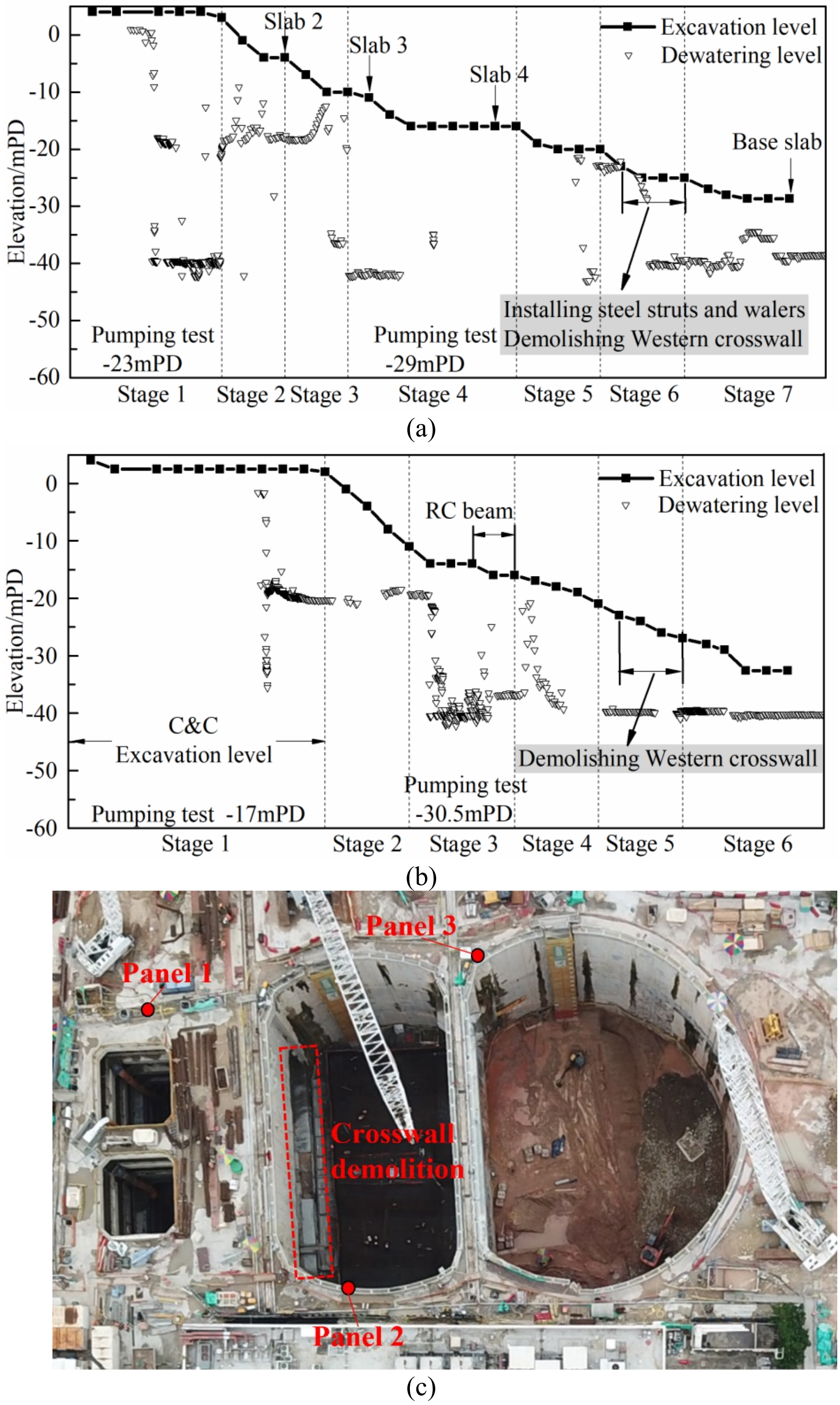

Fig. 2. Construction sequences of (a) the cut-and-cover tunnel section and (b) the twin-circular cofferdam; (c) site photo after excavation

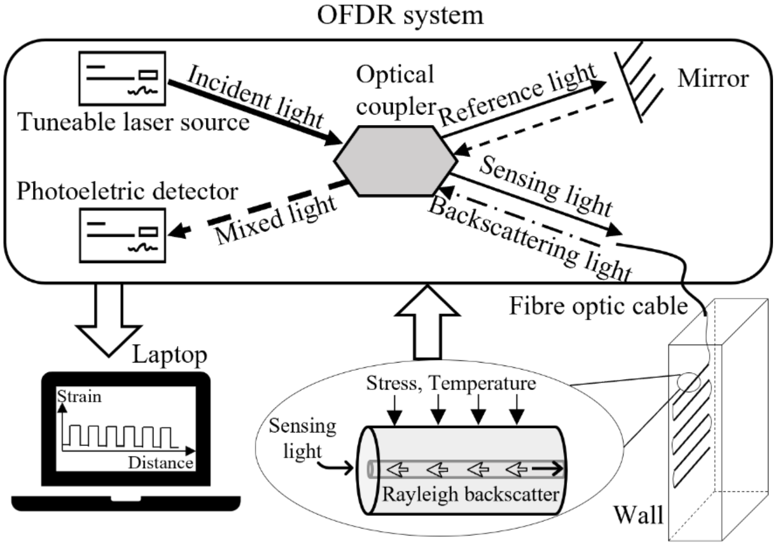

Fig. 3. Working principle of the OFDR

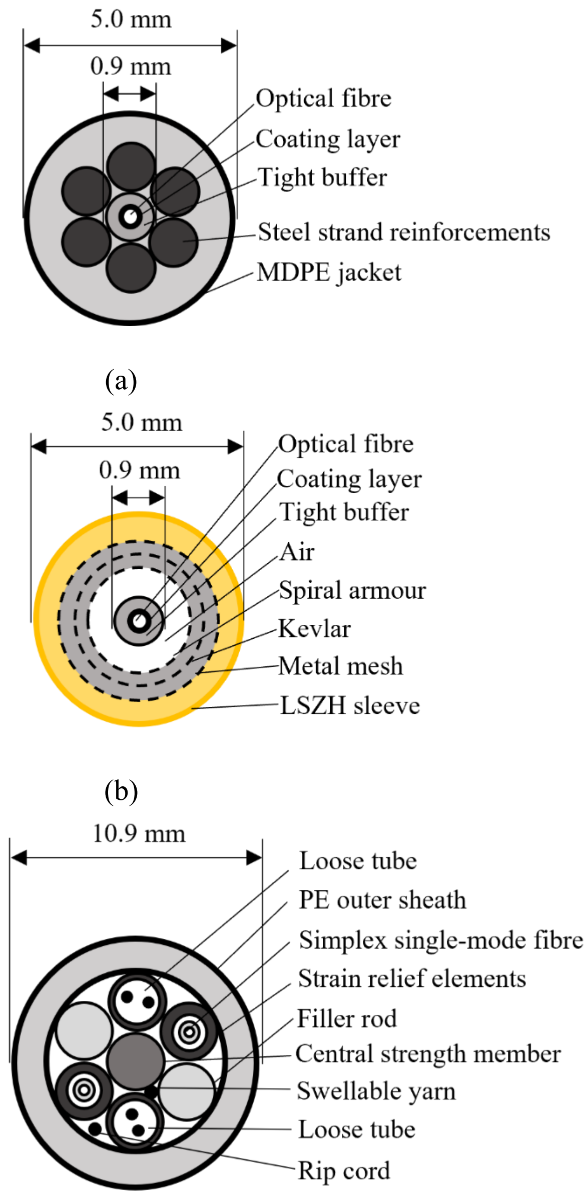

(c)

Fig. 4. Fibre optic cables adopted in the wall monitoring: (a) steel strand-reinforced cable, (b) loose tube cable, and (c) LIOS cable

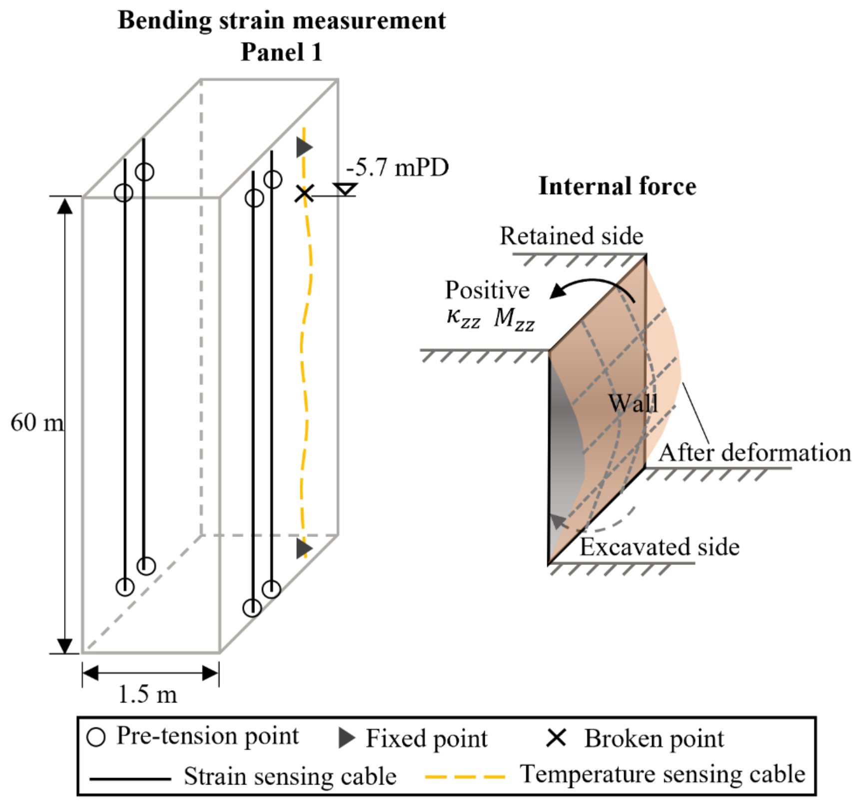

(a) Panel 1

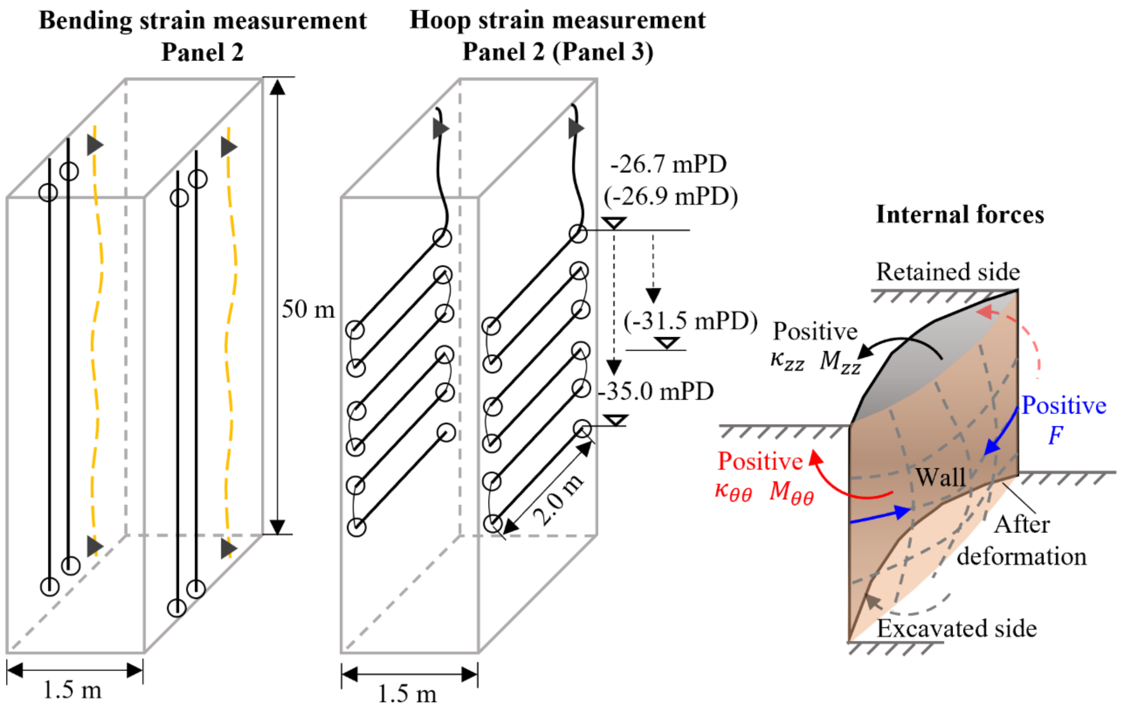

(b) Panel 2 and Panel 3

Fig. 5. Cable arrangements in three diaphragm wall panels and direction indication of the internal forces: (a) Panel 1; (b) Panel 2 and Panel 3

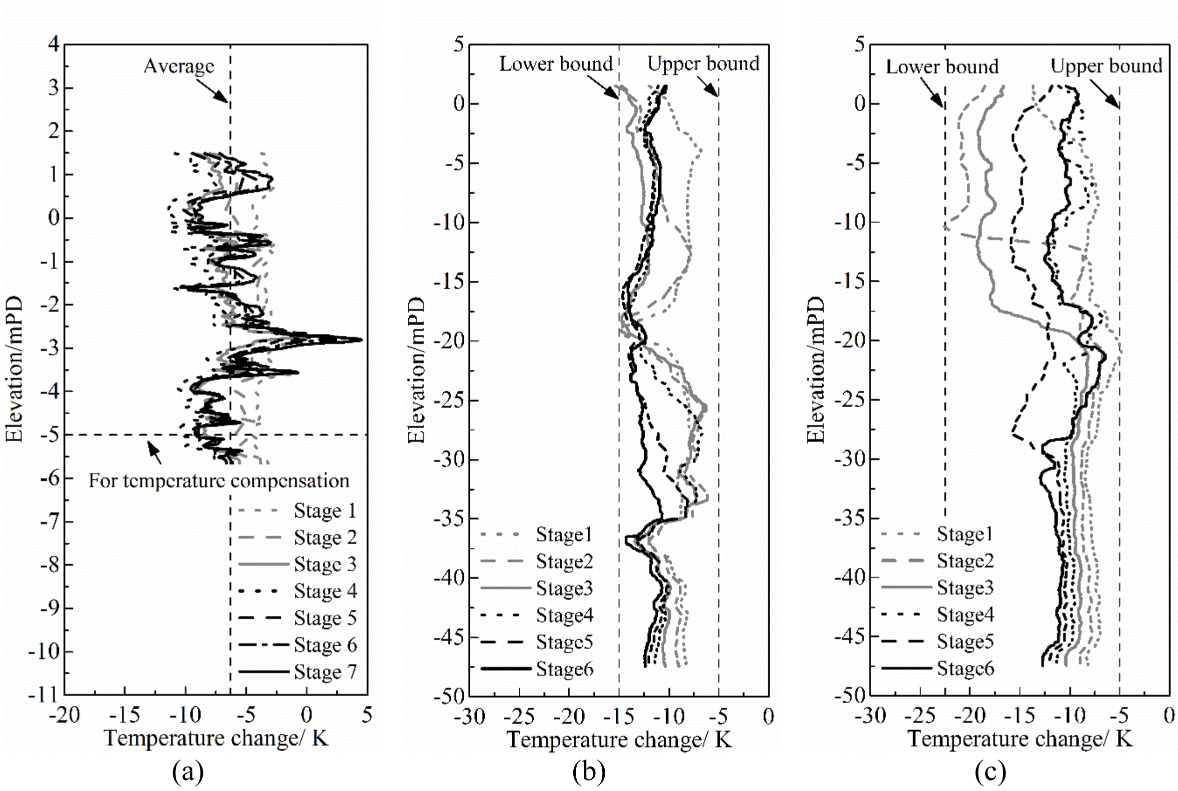

Fig. 6. Temperature changes of wall panels: (a) on the excavated side of Panel 1; (b) on the retained side of Panel 2; (c) on the excavated side of Panel 2

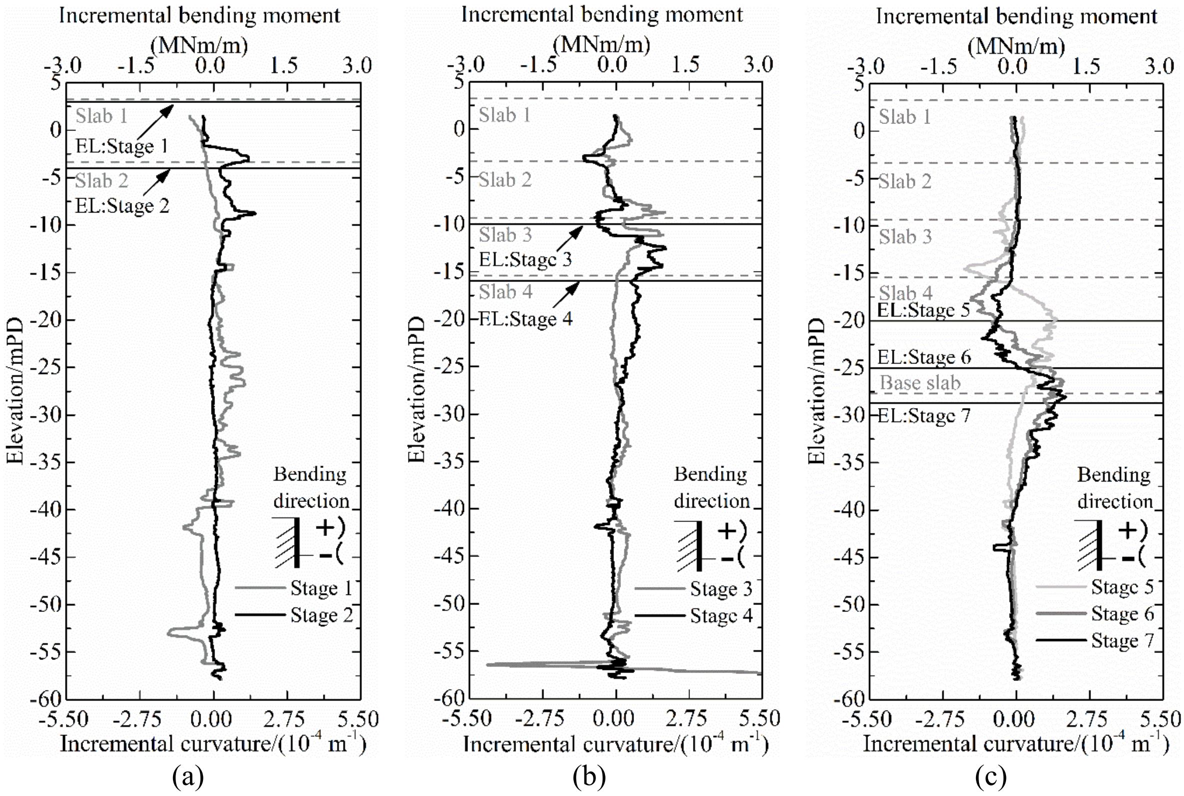

Fig. 7. Curvature and bending moment development in Panel 1: (a) Stage 1 ~ Stage 2; (b) Stage 3 ~ Stage 4; (c) Stage 5 ~ Stage 7 (EL: excavation level)

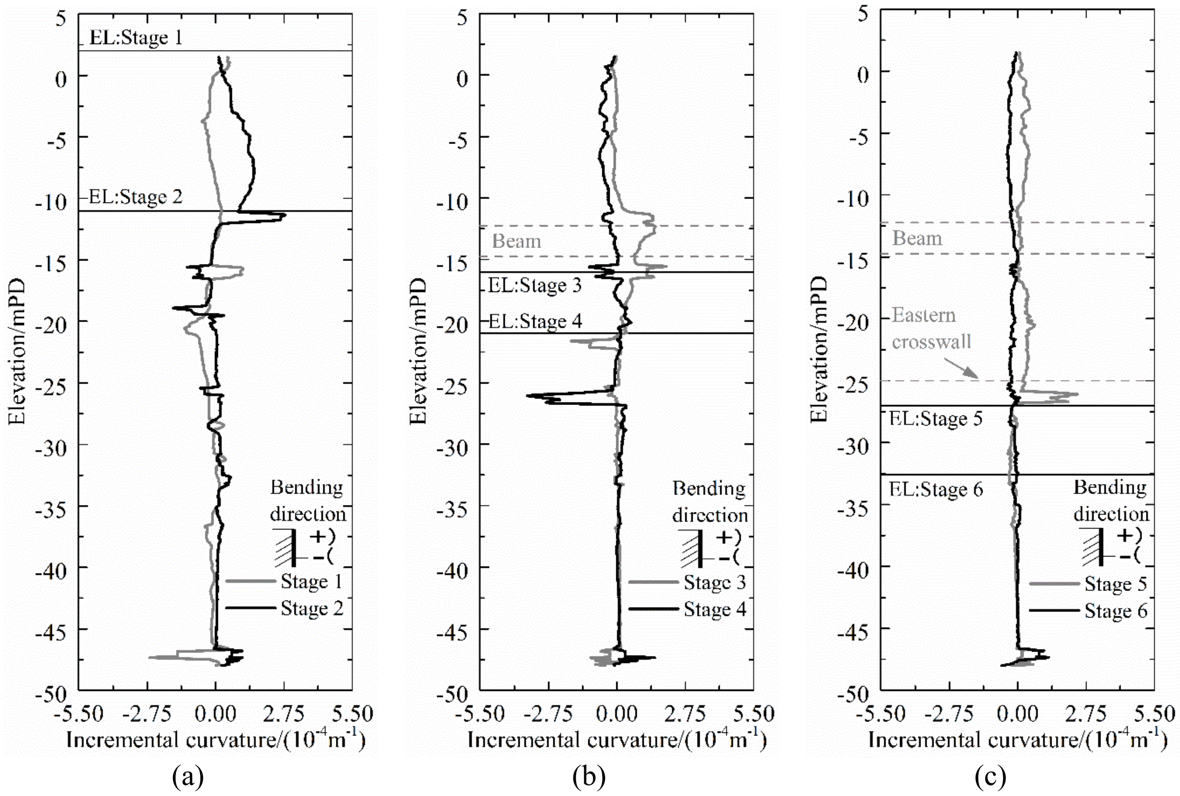

Fig. 8. Curvature development in Panel 2: (a) Stage 1 ~ Stage 2; (b) Stage 3 ~ Stage 4; (c) Stage 5 ~ Stage 6 (EL: excavation level)

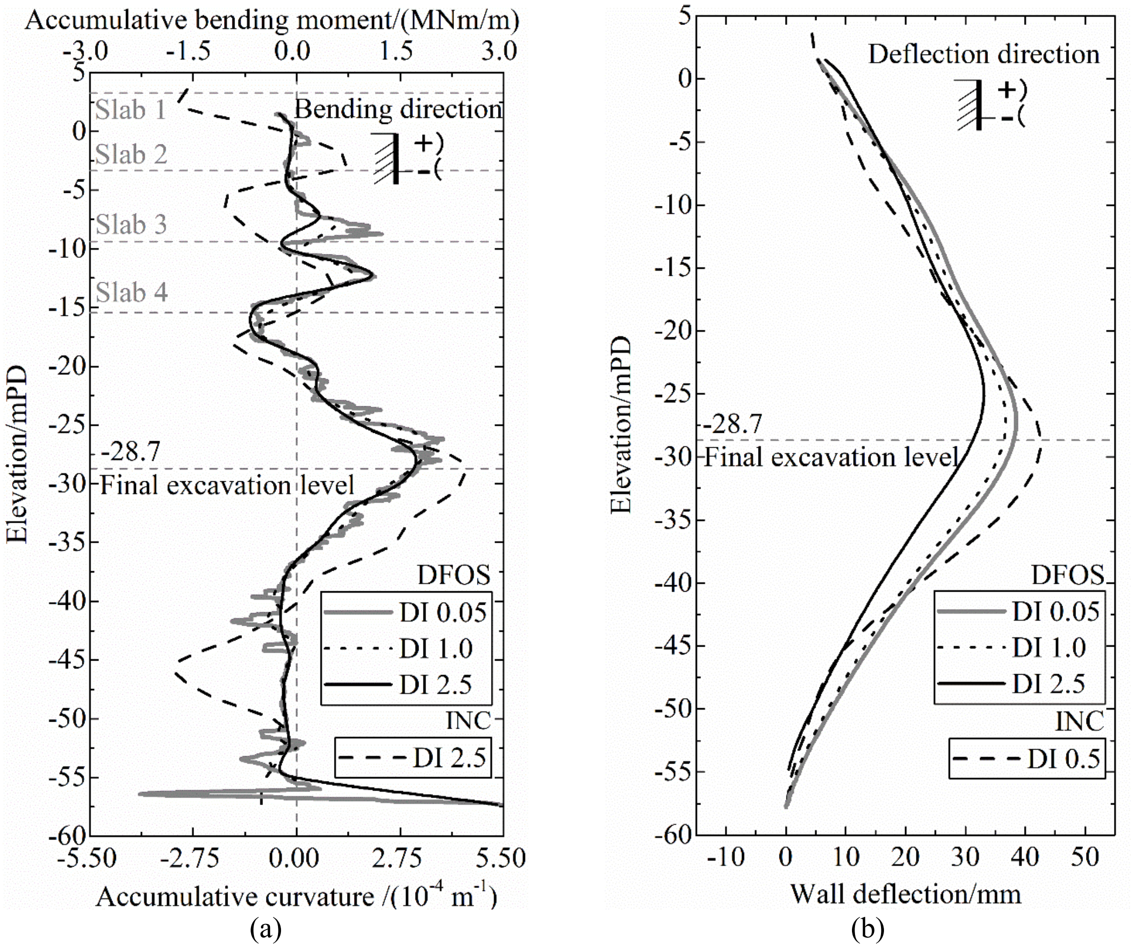

Fig. 9. Comparison of DFOS data and inclinometer results in Panel 1

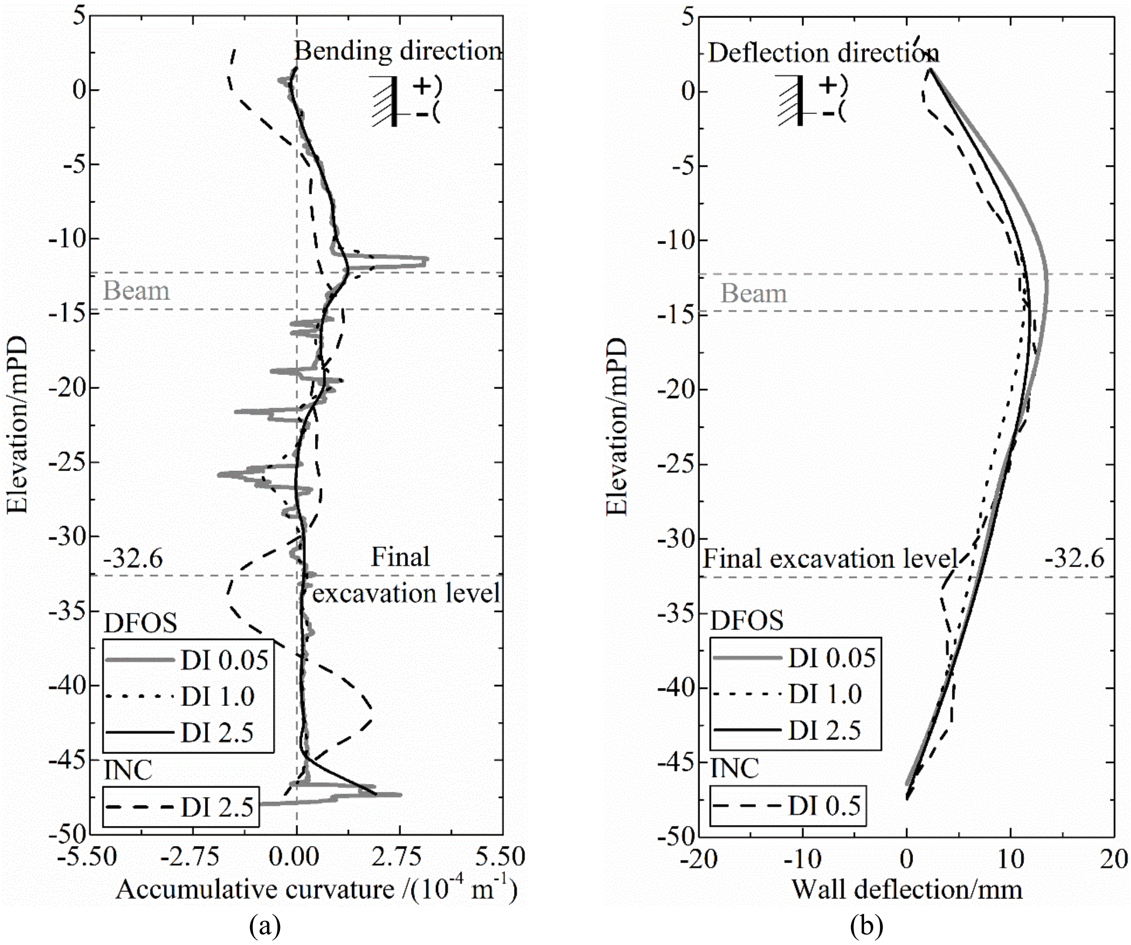

Fig. 10. Comparison of DFOS data and inclinometer results in Panel 2

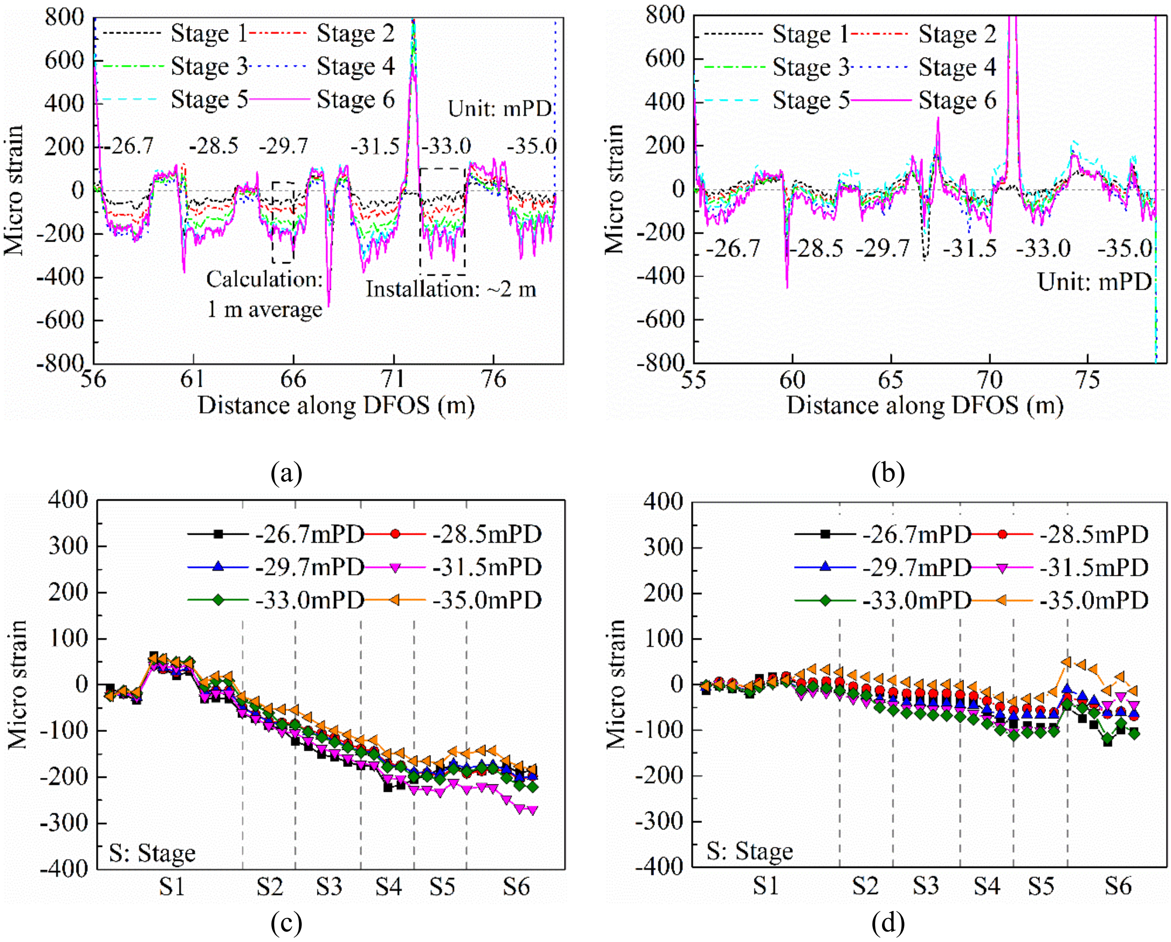

Fig. 11. Hoop strain measurements of DFOS in Panel 2: strain distribution along with sensing distance (a) on the retained side and (b) on the excavated side; strain development during excavation (c) on the retained side and (d) on the excavated side

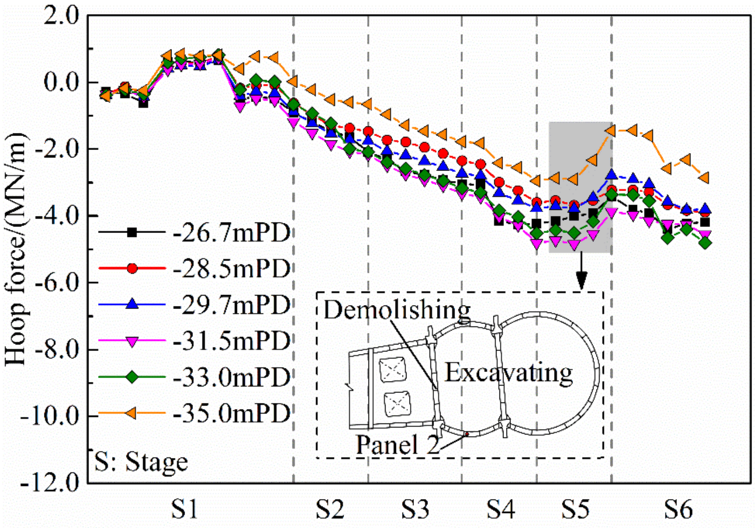

Hoop force/(MN/m)
-26.7mPD
-28.5mPD
-29.7mPD
-31.5mPD
-33.0mPD
-35.0mPD
Demolishing
Excavating
Panel 2
S: Stage
S1
S2
S3
S4
S5
S6

(a)

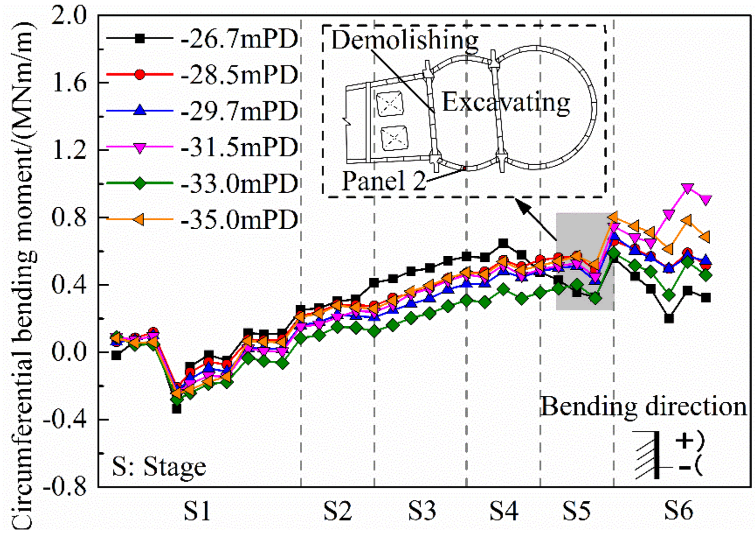

Circumferential bending moment/(MNm/m)
-26.7mPD
-28.5mPD
-29.7mPD
-31.5mPD
-33.0mPD
-35.0mPD
Demolishing
Excavating
Panel 2
Bending direction
S: Stage
S1
S2
S3
S4
S5
S6

(b)

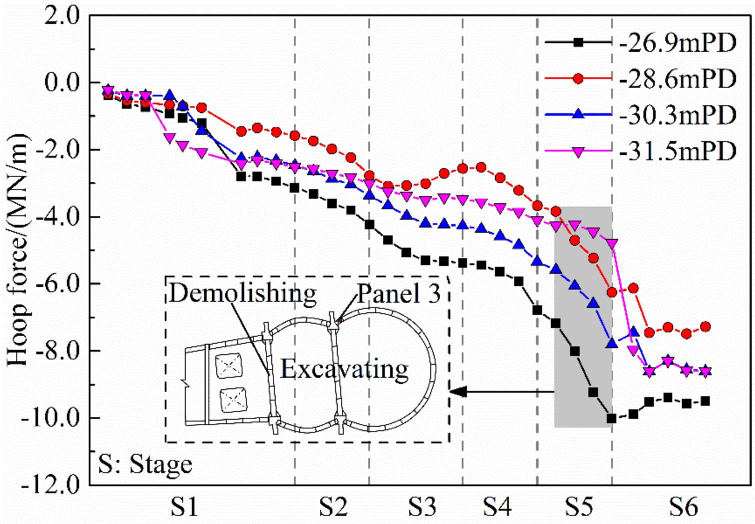

Hoop force/(MN/m)
-26.9mPD
-28.6mPD
-30.3mPD
-31.5mPD
Demolishing
Panel 3
Excavating
S: Stage
S1
S2
S3
S4
S5
S6

(c)

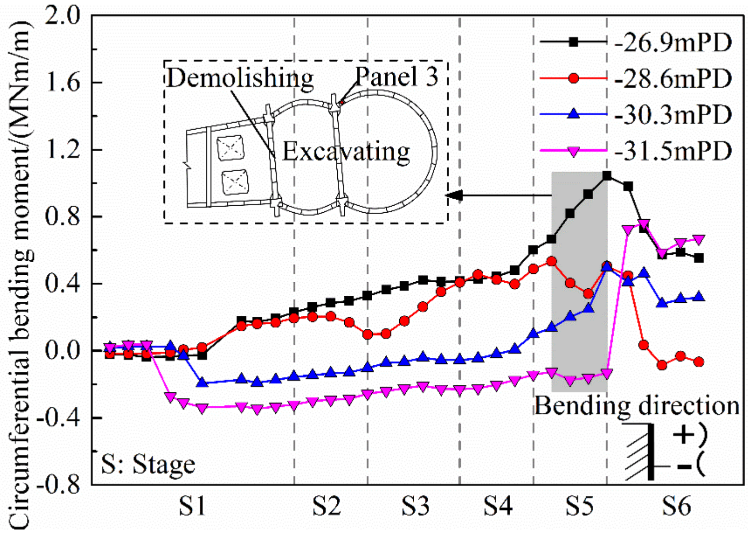

(d)

Fig. 12. Internal forces development: (a) hoop forces in Panel 2; (b) circumferential bending moments in Panel 2; (c) hoop forces in Panel 3; (d) circumferential bending moments in Panel 3

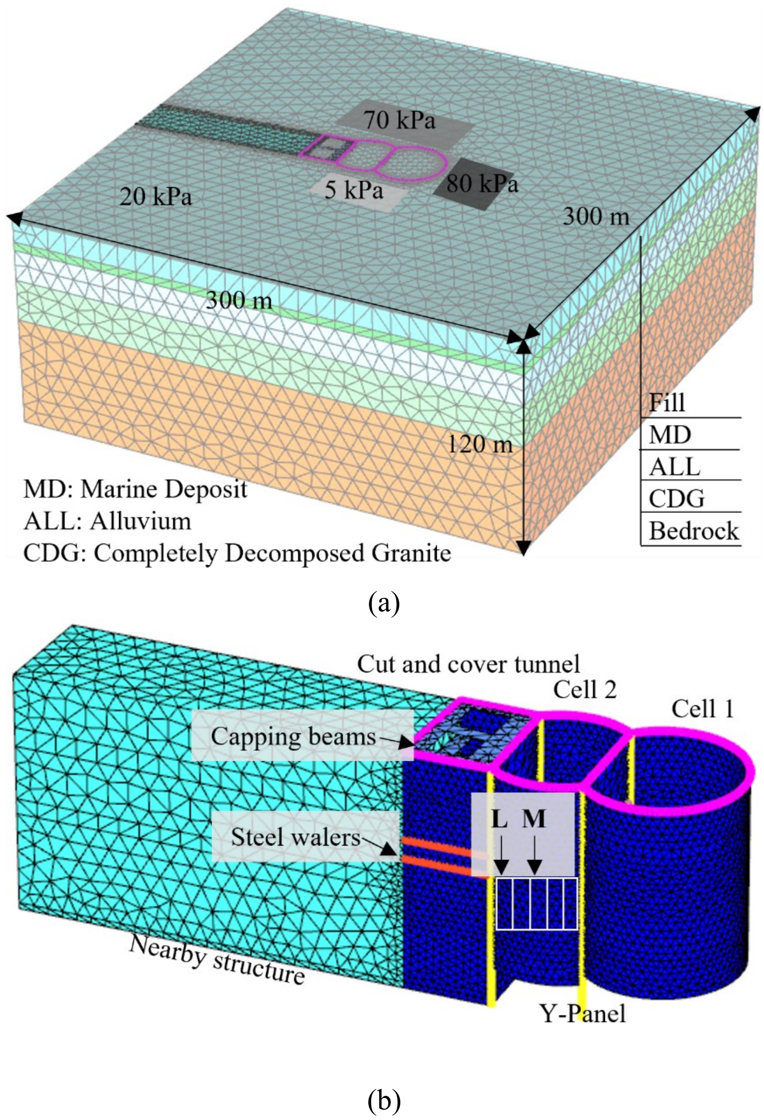

Fig. 13. Overview of the PLAXIS model: (a) stratum and dimensions; (b) structure deformation and data output positions

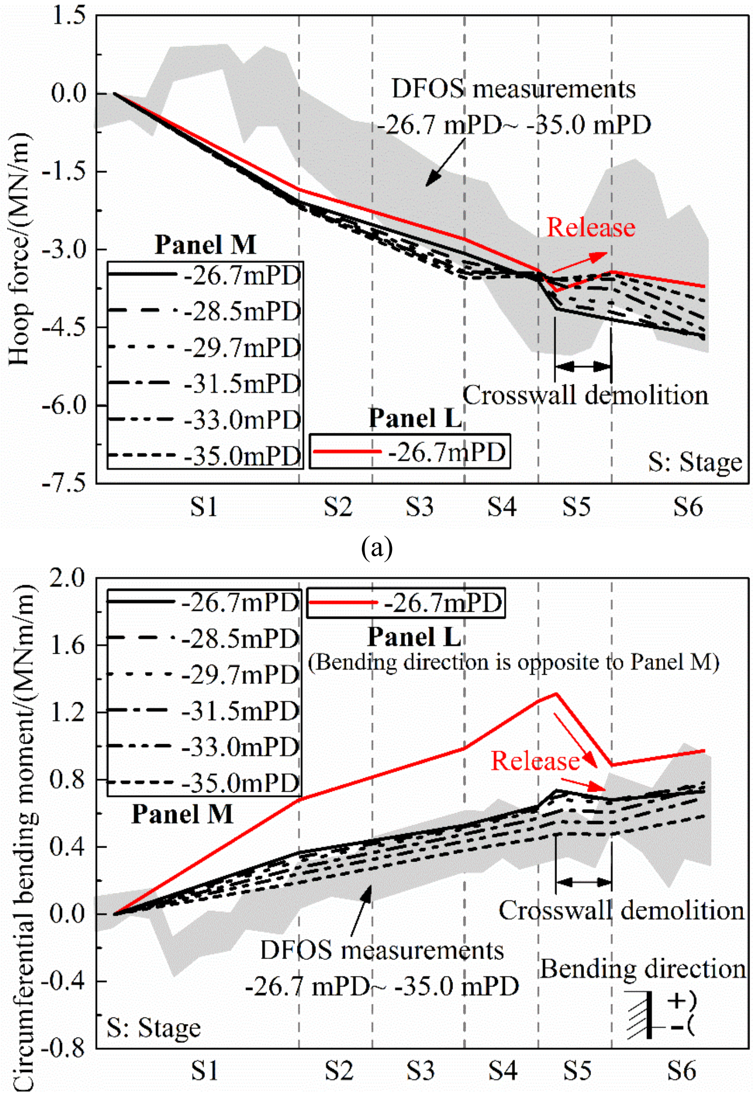

(a)

(b)

Fig. 14. Internal forces development in the benchmark model: (a) hoop force; (b) circumferential bending moment

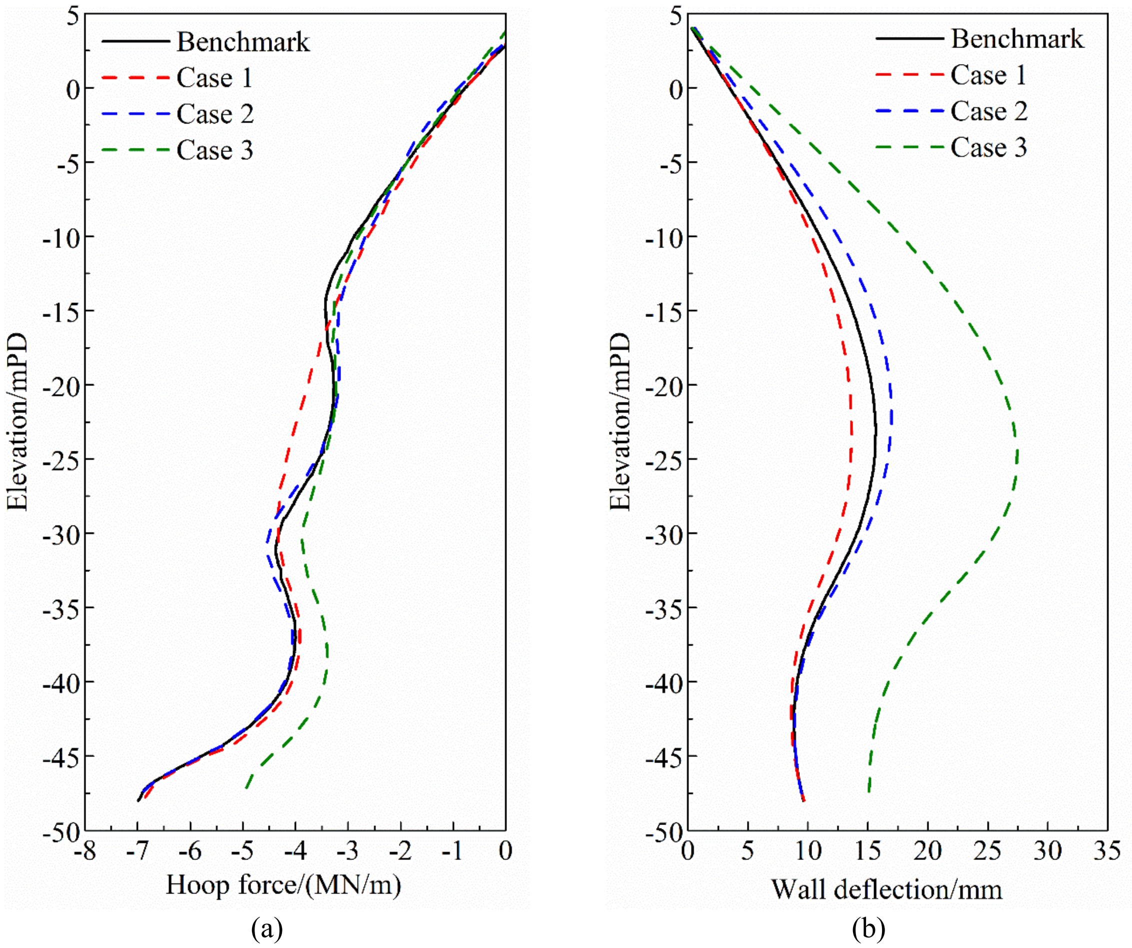

Benchmark
Case 1
Case 2
Case 3
Elevation/mPD
Hoop force/(MN/m)
(a)
Benchmark
Case 1
Case 2
Case 3
Elevation/mPD
Wall deflection/mm
(b)

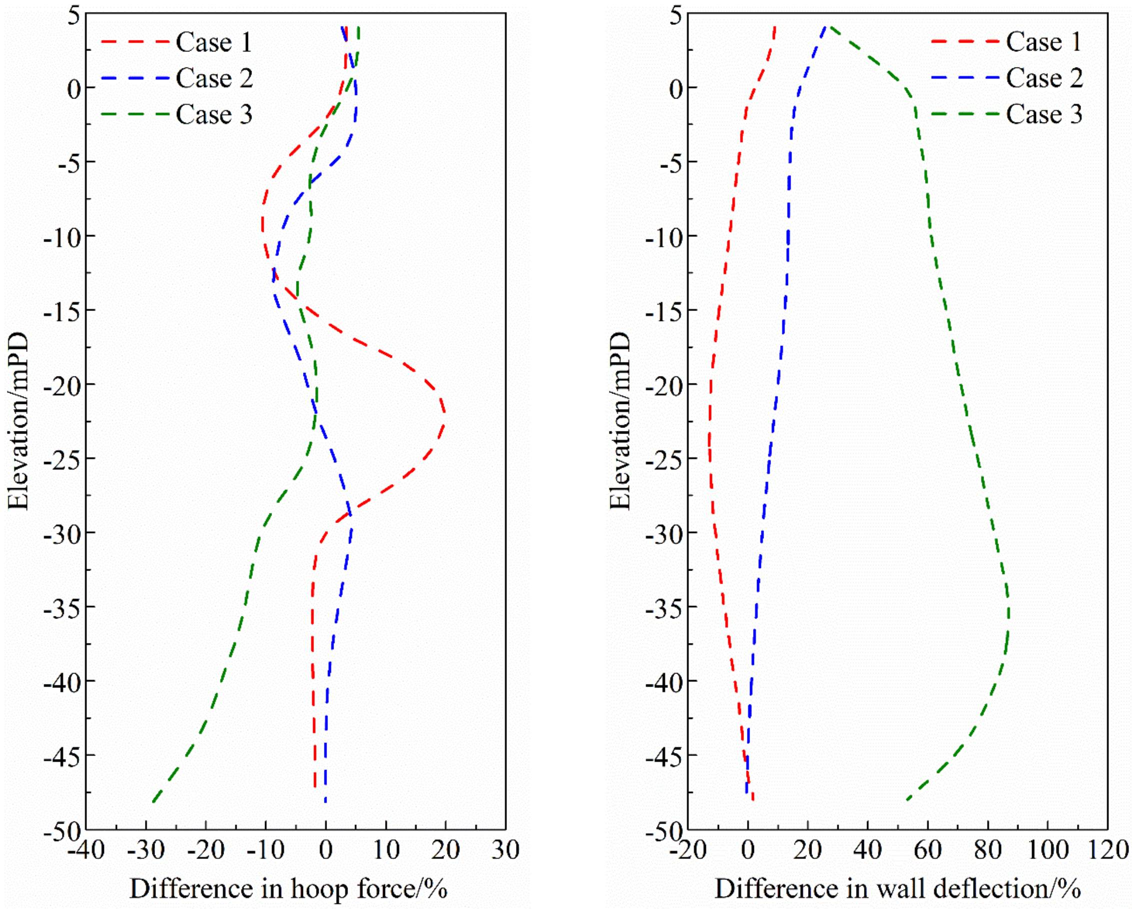

(c) (d)

Fig. 15. Results of four numerical cases at the final stage: (a) hoop force; (b) wall deflection, and difference in (c) hoop force; (d) wall deflection compared to the benchmark model